JOINT EUROPEAN TORUS

JET–P(90)17

G.A. Cottrell, D.F. Start
and JET Team

A Large-Orbit Model for ICRH Heating: Comparison with JET Data

A Large-Orbit Model for ICRH Heating: Comparison with JET Data

G.A. Cottrell, D.F. Start
and JET Team*

JET-Joint Undertaking, Culham Science Centre, OX14 3DB, Abingdon, UK

** See Appendix 1*

Preprint of Paper to be submitted for publication in
Nuclear Fusion

A LARGE–ORBIT MODEL FOR ICRH HEATING: COMPARISON WITH JET DATA

G.A.COTTRELL and D.F.H.START

JET Joint Undertaking, Abingdon, Oxon., OX14 3EA, United Kingdom.

Abstract

Localised and intense Ion Cyclotron Radio Frequency (ICRH) heating of two–ion species plasmas in the Joint European Torus (JET) tokamak produces minority ion distributions having characteristic energies in the multi–MeV range, similar to that of fusion α–particles. For typical values of the poloidal magnetic field, the size of the particle orbits can exceed significantly the width of the RF deposition profile. In the presence of a negative radial gradient in the ion–electron slowing–down time, the finite orbit–width effect gives rise to a significant reduction in the calculated energy content of the minority particles. A model is described which has been compared with RF heating data from the JET tokamak with both hydrogen and ^{3}He minority ion species. The model is capable of explaining previously observed discrepencies between measured fast ion energy contents and those which have been calculated using a zero orbit–width model. The largest corrections to the global energy content of the fast ions are $\approx$ 56% and are found for low–current hydrogen minority cases in which the axial ion–electron slowing–down time is long ($\approx$ 1.5 s). Within the experimental scatter, we have been able to place a upper limit of $D_{fast} \leq 0.18$ m^2 s^{-1} on the fast–ion diffusion coefficient for any non–classical energy–loss processes.

1. INTRODUCTION

During central ICRH heating experiments in large tokamaks such as JET (major radius: $R_0 = 2.96$ m, minor radius: $a = 1.2$ m), the fast magnetosonic wave is focussed on the magnetic axis of the plasma giving rise to large, centrally peaked, densities of RF power in a region of radial extent $\Delta_{rf}/a \approx 0.25$. When a minority ion species absorbs RF power at its fundamental ion cyclotron frequency, its velocity distribution develops a strong non–Maxwellian tail having a characteristic energy ($T_\perp >> T_e$) in the direction perpendicular to the magnetic field where T_e is the thermal temperature of the background

plasma electrons. As the particles move around the drift surfaces, they experience random kicks in energy each time they traverse the cyclotron resonance. Provided the single particle motion is uncorrelated (e.g. by collisions) with the phase of the RF field between successive particle transits through the resonant layer, net energy is gained. This acceleration is balanced against friction which the fast particles experience through Coulomb collisions with the background ions and electrons. In typical ICRH minority heating experiments performed in JET, the ions may, in steady–state, reach energies of several MeV. For particles with such high energies, the vertical guiding centre drift due to magnetic field gradient and curvature cannot be neglected and the ions trace orbits with large radial excursions which can exceed the width of the production profile.

In existing ICRH models, it is generally assumed that the radial width of an orbit is small compared with its mean radial position. Particles trapped in a toroidal magnetic field make radial excursions of up to $\Delta_{orb} \approx \epsilon^{1/2}\, \rho_\theta$ where $\rho_\theta = Mv_\perp / ZeB_\theta$ is the Larmor radius in the poloidal field B_θ [1]. Thus at a given inverse aspect–ratio $\epsilon = r/R$, it becomes necessary to include spatial corrections for the particle orbits when Δ_{orb} is equal to or larger than Δ_{rf}. This condition leads to the existence of a critical characteristic perpendicular minority tail temperature,

$$T_{\perp crit} \approx (\Delta_{rf}\, Z\, B_\varphi / q)^2\, e\, \epsilon\, /2M, \tag{1.1}$$

where the heated particles have charge +Ze and mass $M = Am_p$, B_φ is the toroidal field, the safety factor $q = rB_\varphi/RB_\theta$, m_p is the mass of the proton and e the charge on the electron. Finite orbit effects are therefore important when the the characteristic energy of the heated particles exceeds the critical value given in Eq.(1.1). This particular criterion is perhaps somewhat conservative as finite orbit–width effects will probably be manifested before Δ_{orb} is equal to Δ_{rf}. The critical energy at which ion–ion and ion–electron friction are equal is given by,

$$E_{crit} = [A^{3}/_{2}/n_e\, \Sigma\, n_j Z_j^2 / A_j\,]^{2/3}, \tag{1.2}$$

where the summation extends over all ion species j. In the limit of high particle energy ($T_\perp >> E_{crit}$), the dominant Coulomb process is electron drag which allows one to neglect collisional pitch–angle scattering. Therefore, in the absence of velocity–space instabilities,

the tail can be treated as highly anisotropic ($<v_\perp^2> >> <v_\parallel^2>$) where $v_\perp$ and $v_\parallel$ are, respectively, the perpendicular and parallel velocities of the minority ion. In this limit, the perpendicular energy gained from cyclotron heating is not shared with the parallel degree of freedom so that the coefficient of wave–induced dispersion is increased by a factor of 3/2 over that relevant to the isotropic case. A simple expression then gives the asymptotic perpendicular tail temperature [2],

$$T_\perp = T_e\,(1 + 3\xi_{rf}/2), \tag{1.3}$$

where the Stix parameter ξ_{rf} is,

$$\xi_{rf} = \rho_{rf}\,\tau_s\,/\,3n_{min}\,(kT_e), \tag{1.4}$$

ρ_{rf} is the RF power density coupled to the minority ions and n_{min} the number density of minority ions. In the high energy range, the fast ions suffer collisional energy loss mainly through ion–electron collisions where the rate is characterised by the classical Spitzer momentum slowing–down time,

$$\tau_s = (3\pi^{3/2}\,\epsilon_0^2\,v_{te}^3\,m_e\,M)\,/\,(e^4\,Z^2\,n_e\,\ln\Lambda). \tag{1.5}$$

The electron thermal velocity is v_{te} ($>> (T_\perp/M)^{1/2}$), m_e the electron mass, n_e the number density of electrons and $\ln\Lambda$ the Coulomb logarithm. As a numerical example, let us consider typical conditions close to the axis of the JET tokamak with a set of RF heating parameters relevant to a discharge with high applied ICRH power ($P_{rf} = 12$ MW, $\Delta r_{rf} = 0.3$ m, power density $\rho_{rf} = 2 \times 10^6$ Wm^{-3}) at low density ($n_e = 3 \times 10^{19}$ m^{-3}) with $T_e = 10$ keV, where the ion–electron slowing–down time is large ($\tau_s = 1.3$ sec). Taking protons (A=1, Z=1) as the heated species with concentration $n_{min}\,/\,n_e = 5\%$, and tokamak parameters $B_\varphi = 3.4$ Tesla, $q = 2$, and $\epsilon = 0.07$, Eq.(1.1) gives $T_{\perp crit} = 875$ keV. With the plasma conditions of our example, we find $\xi_{rf} = 360$ giving $T_\perp = 5.4$ MeV which greatly exceeds the $T_{\perp crit}$ threshold.

With central ICRH heating, the radial electron temperature $T_e(r)$ is generally found to be strongly peaked and can be approximated by the fuction,

$$T_e(r) = T_{e_0}\,[1 - x^2]^{\alpha_t}, \tag{1.6}$$

where T_{e_0} is the axial electron temperature and $x = r/a$. Similarly the radial electron density profile can be approximated by,

$$n_e(r) = n_{e_0} [1 - x^2]^{\alpha_n}, \tag{1.7}$$

where n_{e_0} is the axial number density of electrons. The profile of the ion–electron slowing–down time is proportional to $T_e^{3/2} / n_e$, i.e.,

$$\tau_s(r) = \tau_{s_0} [1 - x^2]^{(3\alpha_t/2 - \alpha_n)}, \tag{1.8}$$

where τ_{s_0} is the axial value. In JET ICRH discharges where the MHD sawteeth have been suppressed, the exponent α_t can be as high as 4–8 with $\alpha_n \approx 0.5$. Since the exponent of Eq.(1.8) is high, lying in the range 5.5–11.5 for typical JET data, $\tau_s(r)$ is therefore a strongly peaked function of radius. The average collisional drag experienced by a fast ion over its orbit will therefore increase significantly as its large radial excursion takes it into the cool, outer region of the plasma. If finite orbit–width corrections are neglected for such cases, calculation of the energy distribution of the ensemble of fast ions will seriously under–estimate the energy loss rate and therefore over–estimate the energy of the entire fast ion population.

In some classes of ICRH minority heating experiments it is reasonable to neglect finite orbit effects. Clearly these cases arise when $T_\perp$ falls significantly below $T_{\perp crit}$. Within the span of plasma studies recently conducted on JET, these cases occur for high–density (and high minority density) as well as low RF power experiments. There is also a species effect. Comparing ^{3}He with H minority heating, there is for the ^{3}He ions not only an increase in the $T_{\perp crit}$ limit by a factor $Z^2/A = 4/3$ but also a decrease in the ion–electron slowing–down time by a factor A/Z^2. Thus the energy threshold for ^{3}He ions above which orbit effects are important is effectively raised by a combined factor of $16/9 = 1.78$.

2. ICRH PARTICLE ORBITS IN A TOKAMAK

We start by considering the usual simplified model for the magnetic field of the tokamak,

$$B(\epsilon, \theta) = B_0 (1 + \epsilon \cos\theta), \tag{2.1}$$

where θ is the angle in the poloidal plane. Following earlier analysis [3], the guiding centre orbit can be found from the three invariants of motion, i.e. particle energy,

$$E = 1/2\ M v_{\|}^2 + \mu B_0 (1 - \epsilon \cos\theta), \tag{2.2}$$

magnetic moment, $\mu = M v_{\perp}^2/2B$, and the longitudinal invariant,

$$J = v_{\|} (1 + \epsilon \cos\theta) - \omega_{Ci} R \epsilon^2 / 2q. \tag{2.3}$$

By eliminating $v_{\|}$ from Eqs.(2.2) and (2.3), a quartic equation describing the particle orbit is obtained,

$$(\psi_1^2 + \epsilon \cos\theta) (1 + \epsilon \cos\theta)^2 = (\psi_1 + (\epsilon^2 - \epsilon_1^2) R_0/2\rho q)^2, \tag{2.4}$$

where the pitch–angle $\psi = \psi_1 = (v_{\|}/v_{\perp})_1$ is defined at a reference position: $(\epsilon = \epsilon_1, \theta = \pi/2)$, the Larmor radius in the total magnetic field is $\rho = v_{\perp}/\omega_{Ci}$ and the gyrofrequency is $\omega_{Ci} = ZeB/M$. Eq.(2.4) has been solved numerically generate a family of constant–energy orbits (Fig.1). Note that the banana orbits become D–shaped as the energy increases. For the larger orbits, the return paths pass close to the centre.

2.1 The orbit–averaged slowing–down time

To help illustrate our discussion of orbit–averaged effects, we consider the incremental time the particle spends on its orbit in the radial interval ϵ to $\epsilon + \Delta\epsilon$,

$$\Delta t(\epsilon) = \Delta\epsilon\ /\ (d\epsilon/dt), \tag{2.5}$$

where the component of the drift velocity in the radial direction is,

$$d\epsilon/dt = -v_d \sin\theta \,/\, R_0, \tag{2.6}$$

and the vertical guiding–centre drift velocity due to magnetic field gradient and curvature is,

$$v_d = [v_0^2 - v_{\perp 1}^2 \,/\, 2(1 + \epsilon \cos\theta)] \,/\, \omega_{ci} R_0. \tag{2.7}$$

To demonstrate the difference in behaviour between a normal (thin) banana and a large (D–shaped) orbit, we have calculated the normalized inverse radial velocity for the two extreme orbits in Fig.1, one (the banana) with energy E = 30 keV, the other (the D–shaped orbit) with E = 10 MeV. Results (Fig.2) show that the inverse radial velocity of the normal (thin) banana orbit is symmetric about its mean radial position, $\epsilon_{mean} = (\epsilon_{max} - \epsilon_{min})\,/2$, unlike the case of the large D–shaped orbit. In that case, the particle spends a disproportionately larger amount of time near ϵ_{max}. In the presence of a negative radial gradient in the ion–electron slowing–down time, this asymmetry means that the particle with the D–shaped orbit will experience a relatively higher drag than that which would be calculated at ϵ_{mean}. The orbit–averaged slowing–down time $<\tau_s>$ is given by,

$$<\tau_s> = \oint \tau_s(\epsilon, \theta)\, dt \,/\, \oint dt, \tag{2.8}$$

where the circuital integration is taken over one closed orbit. Using Eq.(1.8) with typical experimental values $\alpha_t = 5$ and $\alpha_n = 0.5$, we have calculated the the ratio $<\tau_s>/\tau_{s_0}$ which we have plotted as a function of particle energy in Fig.3. for the orbit family of Fig.1. As can be seen in Fig.3, the zero orbit–width model is only accurate for particle energies below about 300 keV. Above this energy, the zero orbit–width model significantly over–estimates the value of $<\tau_s>/\tau_{s_0}$.

2.2 The circular orbit approximation

Since the ICRH–generated tail of high energy minority ions principally contains particles with small pitch–angle $\psi << 1$, the tail occupies the deeply trapped region of velocity space. In his analysis of α–particle orbits in a tokamak, Stringer [3] has discovered that certain aspects of the behaviour of a trapped orbit can be approximated by a circular orbit passing through the origin and having the same maximum radius ϵ_{max}. We have tested and used this approximation as the basis of the model described here. In the limit

$\psi << 1$ and at $\theta = 0$, Eq.(2.4) becomes,

$$\epsilon\,(1+\epsilon)^2 = ((\epsilon^2 - \epsilon_1^{\,2})\,R_0/2\rho q)^2, \tag{2.9}$$

from which the maximum radius ϵ_{max} can be found. Further simplification arises by taking the particle velocity to be constant. As Stringer has noted, this is a poor approximation to the poloidal motion. However, like him, we are only interested in the radial variation, particularly near the maximum radius. The circular orbit approximation is poor in the low–energy, thin banana width limit; in this regime, calculations of orbit–averaged quantities can, however, be performed in the zero orbit–width limit. In the circular orbit approximation, the particles spend rather more time near their maximum radii than in the exact case. The fraction of time each particle spends in the normalized radial interval ϵ to $\epsilon + d\epsilon$ is given by,

$$\delta\,(\epsilon) = 2\,/\,\pi\,(\epsilon_{max}^2 - \epsilon^2)^{1/2}, \tag{2.10}$$

and we have plotted the equivalent circular orbit–averaged slowing–down time in Fig.3 together with that for exact orbits. The circular model appears to give a reasonable approximation in the range of typical JET experimental parameters but does tend, however, to underestimate slightly the dwell–time in the low–energy (thin) banana width limit. In this limit, the zero orbit–width model is clearly satisfactory. As we expect, the circular model somewhat over–estimates the dwell–time spent at large radii for the high–energy particles (by $\approx$ 10% for 1 MeV protons rising to $\approx$ 30% for 10 MeV protons). In practice, differences between the two models become less when we consider the expectation value of the orbit–averaged slowing–down time when it has been weighted by a typical ICRH minority distribution function. To illustrate this, we take a form of the steady–state perpendicular energy distribution function (Eq.(38) of ref.[2]) describing the tail in the high–energy limit,

$$f(E_\perp) = \text{constant}\,\exp[-(Mv_\perp^2/2)\,/\,kT_\perp], \tag{2.11}$$

and calculate the expectation value of the orbit–averaged slowing–down time,

$$\overline{<\tau_s>} = \int_0^{v_\perp max} <\tau_s>\, f(E_\perp)\, v_\perp\, dv_\perp \,/\, \int_0^{v_\perp max} f(E_\perp)\, v_\perp\, dv_\perp, \tag{2.12}$$

where $v_{\perp max}$ is the maximum perpendicular velocity of particles which are just confined in the tokamak. The maximum Larmor radius of these particles is,

$$\rho_{max} = R_0 \, (\epsilon_{wall}^2 - \epsilon_i^2) \; / \; [2q \sqrt{\epsilon_{wall}} \, (1 + \epsilon_{wall})]. \tag{2.13}$$

Particles with velocities exceeding $v_{\perp max}$ would have maximum radii ϵ_{max} greater than that of the wall of the torus $\epsilon_{wall} = a/R_0$, and so strike the vessel and are lost. The expectation value $\overline{<\tau_s>}/\tau_{s_0}$ has been plotted in Fig.4 as a function of $T_\perp$. Inspection of Fig.4 shows that the curve based on circular orbits lies $\approx 4\%$ below the exact case for $T_\perp = 1$ MeV. The magnitude of the shortfall increases to $\approx 18\%$ for $T_\perp = 10$ MeV. The degree of error arising from the circular orbit model is, of course, much less than that incurred by taking the conventional zero orbit–width model. In practical terms, we have found the circular orbit model to be both simple to use and fast to compute.

2.3 A self–consistent model of the minority tail

We consider the group of particles born at radii from r to r + dr and seek a self–consistent solution for both $\overline{<\tau_s>}$ and the tail temperature, $T_{\perp sc}$. We can define a self–consistent slowing–down time for the group of particles as,

$$\tau_{sc}(r) = 2 \, n_{min} \, T_{\perp sc}(r) \; / \; \rho_{rf}(r). \tag{2.14}$$

The linear dependence of τ_{sc} on $T_\perp$ has been plotted in Fig.5. Noting, in addition, that $T_\perp$ is coupled to $\overline{<\tau_s>}$ through Eqs.(2.11) and (2.12), we expect to obtain self–consistency when,

$$\tau_{sc} - \overline{<\tau_s>} = 0, \tag{2.15}$$

which is uniquely satisfied at the point of intersection of the two curves illustrated in Fig.5 at the value $T_{\perp sc} = 5.2$ MeV. In this example, the zero orbit–width solution would have given a value $T_\perp = 8.6$ MeV, 65% higher than the self–consistent finite orbit model.

2.4 Further details of the model

For simplicity, we have neglected the finite Doppler broadening of the cyclotron resonance, $\Delta\omega = k_{||}\ \Delta v_{||}$, due to the spread in parallel velocity of the fast ions. This assumption is equivalent to saying that $\Delta v_{||}\ /\ \Delta v_{\perp} << 1$ which means that all the resonant ions lie on the cyclotron resonance chord, $R = R_{res}$. In our model, therefore, the turning points of the trapped banana and D–shaped orbits are assumed to lie on this chord. In earlier JET experiments [5], the temporal response of the plasma to modulated RF heating power has been measured. Results show that, for centrally heated H and ^{3}He minority plasmas, the RF deposition can be approximated by a radial Gaussian function with characteristic e–folding radius $r_d = 0.3 \pm 0.05$ m. In our present model we have therefore represented the coupled RF power deposition profile with a Gaussian,

$$\rho_{rf}(r) = \rho_{rf_0} \exp[-(r - r_{oa})^2/r_d^2], \tag{2.16}$$

where $r_{oa} = |\, R_0 - R_{res}|$ is the (off–axis) radial displacement of the cyclotron resonance from the magnetic axis. The axial value of the RF power density coupled to the minority ions is,

$$\rho_{rf_0} = P_{rfc}/C, \tag{2.17}$$

where P_{rfc} is the total RF power coupled to the minority ions and the normalization constant is given by,

$$2C = r_d^2\ \{\exp[-(r_{oa}/r_d)^2] - \exp[-(a - r_{oa})^2/{r_d}^2]\} +$$

$$+\ r_{oa} r_d \sqrt{\pi}\ \{\mathrm{erf}[(a - r_{oa})/r_d] - \mathrm{erf}[r_{oa}/r_d]\}. \tag{2.18}$$

RF modulation experiments also allow the fraction $\mu = P_{rfc}/P_{rf}$ of the applied RF power coupled to the minority species to be determined. For centrally heated H and ^{3}He minority heating, the experimental value $\mu = 0.65 \pm 0.1$ is typical and we have adopted this in the analysis of the JET discharges below. The remaining power fraction $(1 - \mu)$ is attributed to mode conversion, Landau damping and TTMP.

The self–consistent minority tail was calculated in each incremental radial shell

using the form for the RF power deposition above and electron temperature and density profiles (Eqs.(1.6) and (1.7)) fitted to measured tokamak data. In our model we have taken the number density of minority ions to be constant fraction $\eta = (n_{min}/n_e)$ of the electron density. An example of the calculation based on data from a 2 MA, 2.1 Tesla (H)D discharge is shown in Fig.6. The largest orbital corrections in this case were in the central region, out to a radius of 0.37 m. The large orbit–width model gave corrections which reduced the axial tail temperature by as much as 56% on the axis compared with the zero orbit–width limit. Beyond the radius r = 0.37 m the RF power density had dropped to a sufficiently low level such that the orbits no longer possess the D–shaped character and so could be described accurately in the zero orbit–width limit. Having determined the self–consistent asymptotic tail temperature, $T_{\perp sc}$, in each incremental radial shell, we calculated the total fast ion energy content in this shell using the expression,

$$W_{calc} = 8\pi^3 R_0 \int_0^a r\, n_{min}\, kT_{\perp sc}\, dr. \qquad (2.19)$$

For typical JET data, the fraction of energetic minority particles lost by direct interception with the wall is negligible. We have then compared W_{calc} with the measured fast ion energy content of a number of plasmas obtained in JET.

3. COMPARISON WITH ICRH DATA ON JET

The JET ICRH heating system [4] consists of eight antennae arranged around the median plane of the machine. The antennae are polarized to launch the fast magnetosonic wave from the low–field side of the plasma and consist of pairs of Faraday–screened conductors which can be phased to create either monopole or toroidal dipole configurations and thus change the $k_{||}$ spectrum. In the experiments reported here, the monopole configuration was used. This produces a broad $k_{||}$–spectrum, centered about $k_{||} = 0$. In each of the discharges analysed, the RF frequency was chosen to give central heating with the fundamental minority resonance located within ± 0.1 m of the magnetic axis.

The perpendicular part of the energy of the ICRH–driven fast ions (W_{fast}) in excess of the isotropic component is deduced from the total plasma energy derived from the magnetic equilibrium W_{mhd}, and the total plasma energy derived from diamagnetic measurements W_{dia},

$$W_{fast} = 4/3\ (W_{dia} - W_{mhd}). \tag{3.2}$$

This technique is clearly insensitive to heating regimes in which the fast ions have an isotropic velocity–space distribution. Such cases arise in the low–energy range ($E \approx E_{crit}$) where ion–ion pitch–angle scattering destroys the anisotropy of the tail. We have therefore selected discharges in the high–energy range ($T_{\perp} >> E_{crit}$) for the present study. The method of using Eq.(3.2) to determine fast ion energy contents is, in practice, sensitive to the presence of baseline offsets both in W_{dia} (through calibration errors) and in W_{mhd} (through, for example, non–equilibrium conditions). We have, therefore, been particularly careful to choose steady–state discharge conditions in the data sets analysed; in particular, we have avoided possible sawtooth–induced fast–ion redistribution effects by selecting sawtooth–free discharges where no sawteeth appear for periods ≈ a few × τ_{S0}. In addition, we have been careful to search for systematic baseline offsets in the data; where possible, we have checked that $(W_{dia} - W_{mhd}) = 0$ at suitable times both before and after application of the ICRH heating pulse. This is tantamount to assuming the content of superthermal ions to be negligible during ohmic heating phases of the discharge. Errors in determining the total fast ion energy content have been estimated to be approximately ± 20%. The total plasma energy is given by,

$$W_{tot} = W_{\perp} + W_{||} = (2W_{mhd} + W_{dia})/3. \tag{3.3}$$

The time–evolution of the main plasma parameters of a hydrogen minority (H)D limiter discharge is shown in Fig.7. By comparison with similar discharges in which the low–energy channels of a neutral particle analyser have been used to determine the hydrogen minority concentration, we expect typically $\eta \approx 5\%$ in this discharge. By applying the ICRH power early in the current rise phase of the discharge, it has been found that the onset of sawtoothing activity can be delayed in high current JET discharges. In the discharge of Fig.7, the plasma current attained its maximum (steady) value of 5 MA at time t = 5 sec. After the initial time–varying period, measurements of the plasma energy are reliable (t > 5 sec) and coincide with a suitable sawtooth–free period (from 5.2–6.5 sec). The measured plasma parameters are given in Table I. Note that in this case the fast ion energy content reaches about 50% of the total plasma energy.

We have examined relevant JET discharges, meeting the criteria outlined above, for orbital effects related to the energetic ions. The important experimental parameter in this

survey is the ratio: P_{rf}/n_{e_0}. Previous scaling studies [6] have shown that, for centrally heated discharges, both the ion and electron temperatures increase monotonically with this ratio and Eq.(1.5) for τ_s indicates the fundamental importance of P_{rf}/n_{e_0} in determining the magnitude high–energy ion population. Furthermore, the tail temperature depends sensitively both on τ_s and ρ_{rf} (from the Stix parameter, Eq.(1.4)). Thus we would expect the most prominent finite orbit effects to occur for discharges in which the ratio P_{rf}/n_{e_0} is large and the plasma current is small. In both (H)D and (^{3}He)D experiments performed in 1988, the tokamak limiter material was Carbon. Control of the rise in plasma density with C–limiters was generally difficult to obtain, although some control could be obtained after extensive glow discharge cleaning and conditioning with helium. Typically with high–power ICRH heating ($P_{rf} \approx$ 10–14 MW) ratios of $P_{rf}/n_{e_0} < 3.8$ MW 10^{-19} m^3 were obtained. In 1989, the C–limiters were replaced by Be–limiters and Be was evaporated on the ICRH antenna screens. This led to an enhancement in the torus pumping rate which improved the density control during plasma operation. With similar ICRH powers in Be–torus experiments, the axial electron densities were generally lower giving an extended range of the ratio: $P_{rf}/n_{e_0} < 5.4$ MW 10^{-19} m^3. We have examined data covering both of these modes of operation. The groups of data are summarized in Table II.

3.1 Comparison of zero– and finite orbit–width models with experimental data

For each discharge in the groups A–F, the calculated fast ion energy (W_{calc}) was determined using both the zero and finite orbit–width models. With data of both minority heating schemes, the value $\mu = 0.65$ was taken. Results for the (H)D data set are shown in Fig.8 (a) and (b). Note the data saturation, particularly severe in the case of the 2MA discharges. The highest energy 2MA point has $\tau_{s_0} \approx 1.5$ s, similar to that of the 5MA data group. Results for the (^{3}He)D data set are shown in Figs.9 (a) and (b). As noted in section 1, the critical tail energy above which orbit effects become significant is larger for ^{3}He than for H minority ions. This is one reason why the magnitude of the orbit corrections shown in Figs.9 (a) and (b) for the (^{3}He)D data are generally smaller than those for the (H)D cases of Fig.8. Another reason is the fact that, for the 2 MA and 3.2 MA (^{3}He)D discharges (groups A and B with C–limiters), the plasma density was typically higher (by a factor $\approx$ 1.5) than for the (H)D discharges. The largest corrections in the (^{3}He)D data set are for the 3 MA group. This subset was obtained at relatively lower plasma density and corresponds to operation with the Be limiters.

In view of the fact that reasonable agreement has been obtained between our classical finite orbit–width model and existing JET data, it is of interest to enquire as to the magnitude of any additional fast ion energy loss mechanisms which may be present. To answer this question, we have considered the time–dependent fast ion energy equation,

$$dW_{fast} / dt = P_{rfc} - W_{fast} (2/<\tau_{sc}> + 1/\tau_{loss}), \qquad (3.4)$$

where $<\tau_{sc}>$ is the average self–consistent ion–electron momentum slowing–down time and we have included an new, additive energy–loss term with characteristic time τ_{loss}. In steady–state we obtain,

$$W_{fast} = P_{rfc} (<\tau_{sc}> \tau_{loss}) / (2\tau_{loss} + <\tau_{sc}>), \qquad (3.5)$$

which we have used to examine the effect of different assumed values of τ_{loss} on the quality of fit between the experimental data and the model. Taking the hydrogen minority data shown in Fig.8(b), which corresponds to of $\tau_{loss} = \infty$, and computing the value of the goodness–of–fit statistic χ^2, we decreased the assumed value of τ_{loss} until χ^2 was doubled. This, we found, occurred when $\tau_{loss} \approx 2$ s. Thus any additional fast ion energy loss processes probably take place with a timescale longer than this. Given this lower limit, it is possible to estimate an upper limit on the fast ion diffusion coefficient,

$$D_{fast} = a^2 / 4\tau_{loss}, \qquad (3.6)$$

for which we find $D_{fast} \leq 0.18$ m^2 s^{-1}. The result is, however, somewhat sensitive to the assumed minority ion concentration, η. We have therefore examined the sensitivity of the finite orbit–width calculation of the global fast ion stored energy with respect to variations in η for two extreme experimental cases, the 5 MA and the 2 MA proton minority data with $\tau_{s0} \approx 1.5$ s. By both doubling and halving the assumed concentration ratio about a nominal value of $\eta = 5\%$ (keeping all other parameters constant) we found, respectively, variations in W_{calc} of + 5% and − 6% (at 5 MA) and of + 8% and − 7% (at 2 MA). We note that the magnitude of these variations are smaller than the estimated uncertainties in the measurement of W_{fast} (± 20%).

4. SUMMARY

In JET (H)D ICRF minority heating experiments, near steady–state plasmas contain up to ≈50% of the total plasma energy in the form of fast ions ($W_{fast} \approx 2.4$ MJ, equivalent to a volume–averaged beta $\beta \approx 0.8\%$). With particle energies in the MeV range and central ion–electron slowing–down times $\tau_{s_0} \leq 1.5$ s, these discharges contain fast particle distributions in which the finite size of the particle orbits cannot be neglected. The plasmas also simulate many aspects of α–particle heating. Apart from velocity–space anisotropy ($W_\perp >> W_{||}$) assuming no relaxation due to velocity–space instabilities, the fast ions possess the main features of α–particles in an ignited plasma [7,8]. Our analysis has shown that, provided due allowance is made for the finite orbit–width effects, such discharges may be reasonably well described by classical orbit and slowing–down theory. Within the uncertainties of the experimental measurements and the limitations of the simulation, we conclude therefore that there is no evidence for any anomalous energy–loss processes for high energy particles in JET sawtooth–free discharges. In fact, we have been able to set a upper limit of $D_{fast} \leq 0.18\ m^2\ s^{-1}$ on the diffusion coefficient corresponding to any anomalous fast ion energy losses. The lower limit for the corresponding anomalous energy–loss timescale of $\tau_{loss} \approx 2$ s lies in the upper part of the range of values expected for the slowing–down time of α–particles in a reactor.

Measurements of the electron heating after a sawtooth crash [9] in JET have shown that only about 50% of the energy content of the fast ions is retained in the centre of the plasma. Earlier JET measurements of 15 MeV D–^{3}He fusion protons have shown fast ion ejection from the column during normal sawtooth activity. To investigate the particle loss mechanism (for example the role of helical MHD structures and orbit stochastization), future studies will include experiments on the interaction of fast particles with MHD activity with particular emphasis on particle trapping and loss in the approach to the tokamak β–limit.

ACKNOWLEDGEMENTS

It is a pleasure for the authors to thank P. van Belle for computing advice during development of the model used here as well as Drs. J.Jacquinot, W.Core and L.G.Eriksson for discussions.

REFERENCES

[1] KADOMTSEV, B.B. and POGUTSE (1967), O.P. Soviet Phys. JETP **24**, 1172.

[2] STIX, T.H. (1975), Nucl. Fusion **15**, 737.

[3] STRINGER, T.E. (1974) Plasma Physics **16**, 651.

[4] JACQUINOT, J., BHATNAGAR, V., BRINKSHULTE, H. et al. (1987), Philos. Trans. R. Soc. Lond., Ser. A **322**, 3.

[5] START, D.F.H., EVRARD, M.P., BHATNAGAR, V.P. et al. (1990), to be submitted to Plasma Physics and Controlled Fusion.

[6] BOYD, D.A., CAMPBELL, D.J., CORDEY, J.G. et al. (1989) Nucl. Fusion **29** 593.

[7] POST, D., HWANG, D., MIKKELSEN, D., SEIDL, F. (1983) J.Vac.Sci.Technol. **A1(2)**, 206.

[8] THOMAS, P.R. and THE JET TEAM (1988) IAEA Twelfth International Conference n Plasma Physics and Controlled Nuclear Fusion. **IAEA–CN–50/A–4–4**

[9] ERIKSSON, L.–G., HELLSTEN, T., BOYD, D.A. et al., (1989) Nucl. Fusion **29** 87.

TABLE I

Measured parameters for discharge No. 20371 at time t = 6 sec

Axial Toroidal field	$B_{\varphi}(0) = 3.1$ Tesla
Plasma current	$I_p = 5.0$ MA
Coupled RF power	$P_{rf} = 8.8$ MW
RF frequency	f = 48 MHz
Antenna phasing	monopole
Axial electron density	$n_{e_0} = 2.8 \times 10^{19}$ m^{-3}
Ratio: RF power–to–axial density	$P_{rf}/n_{e_0} = 3.1$ MW 10^{-19} m^3
Axial electron temperature	$T_{e_0} = 11.1$ keV
Axial ion temperature	$T_{i_0} = 6.5$ keV
Axial ion–electron slowing–down time	$\tau_{s_0} = 1.65$ sec
Diamagnetic stored energy	$W_{dia} = 6.36$ MJ
Equilibrium stored energy	$W_{mhd} = 4.63$ MJ
Anisotropic stored energy	$W_{fast} = 2.30$ MJ
Total plasma energy	$W_{tot} = 5.20$ MJ
Ratio: anisotropic–to–total energy	$W_{fast}/W_{tot} = 44\%$

TABLE II

Summary of plasma parameter ranges for the data analysed†

Group	I_p (MA)	B_{φ}(T)	P_{rf}(MW)	$n_{e_0}(10^{19}$m$^{-3})$	T_{e_0}(keV)
A. (^{3}He)D	3.3	3.3	< 13.8	4.2–5.9	4.2–9.5
B. (^{3}He)D	3.0	3.2	< 13.5	3.1–5.3	6.1–9.0
C. (H)D	5.0	3.1	< 11.1	2.7–3.0	10.6–11.1
D. (H)D	3.0	2.1	< 8.5	3.3–4.8	6.2–9.2
E. (H)^{3}He	2.0	2.1	< 11.7	1.8–3.4	5.6–9.3
F. (^{3}He)D	3.0	3.2	< 9.6	3.3–4.6	5.2–8.2

†Groups A, B, C and D contain data from Carbon limiter experiments. Groups E and F contain data from experiments with Be limiters and gettering.

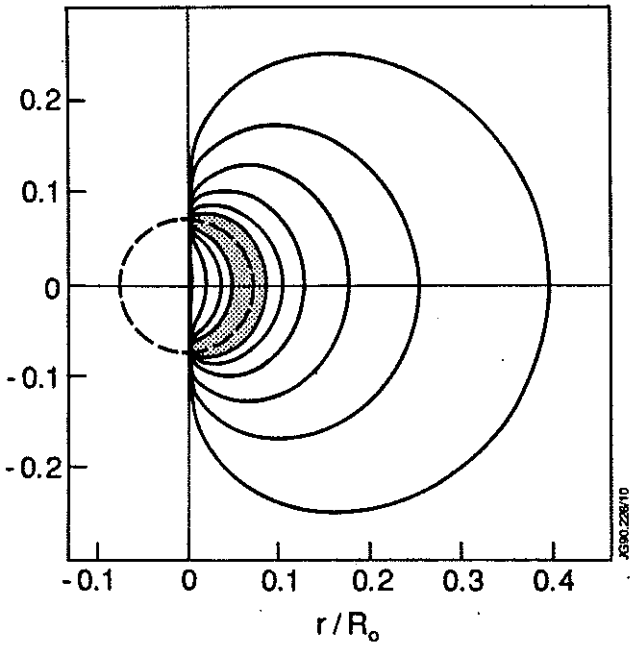

Fig.1. Set of guiding–centre proton orbits shown in poloidal projection obtained by solution of Eq.(2.4). The parameters are: $\epsilon_1 = 0.07$, $\psi_1 = 0$, $B_\varphi = 3.4$ Tesla and $q = 2$. The circular birth flux surface is shown by the dashed line. Starting from the smallest orbit (hatched) upwards the energies are: E = 30 keV, 100 keV, 300 keV, 1 MeV, 3 MeV and 10 MeV. Note the morphological transition from a normal 'banana' to a large D–shaped orbit which occurs above an energy of about 300 keV.

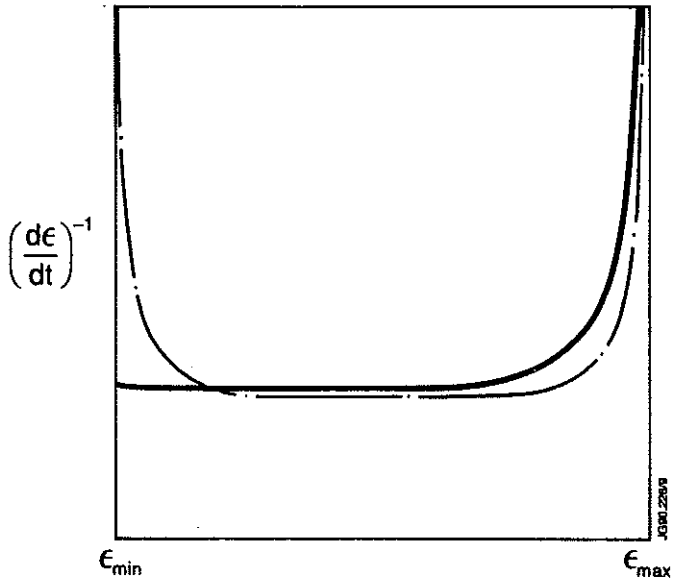

Fig.2. Plot of the relative time (inverse radial velocity) spent by a fast ion at normalised radius ϵ for, broken line: the 30 keV thin banana and, solid line: the 10 MeV D–shaped proton orbits of Fig.1. The curves have been plotted as a function of radius, ϵ, between the minimum (ϵ_{min}) and maximum (ϵ_{max}) radii of the orbital excursion. Both curves have also been normalized to the same area for comparison.

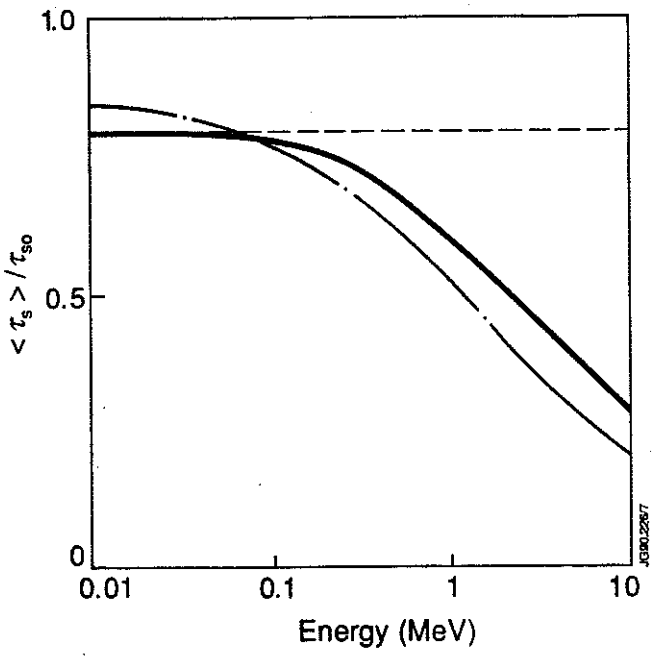

Fig.3. Plot of the normalized orbit–averaged slowing–down time, $<\tau_S>/\tau_{S_0}$ as a function of particle energy for the family of proton orbits in Fig.1 and based on the same set of parameters. Solid curve: exact guiding–centre orbit calculation, broken curve: the circular orbit approximation. The horizontal dashed line at $<\tau_S>/\tau_{S_0} = 0.79$ represents the zero orbit–width model (calculated here at $\epsilon = 0.07$).

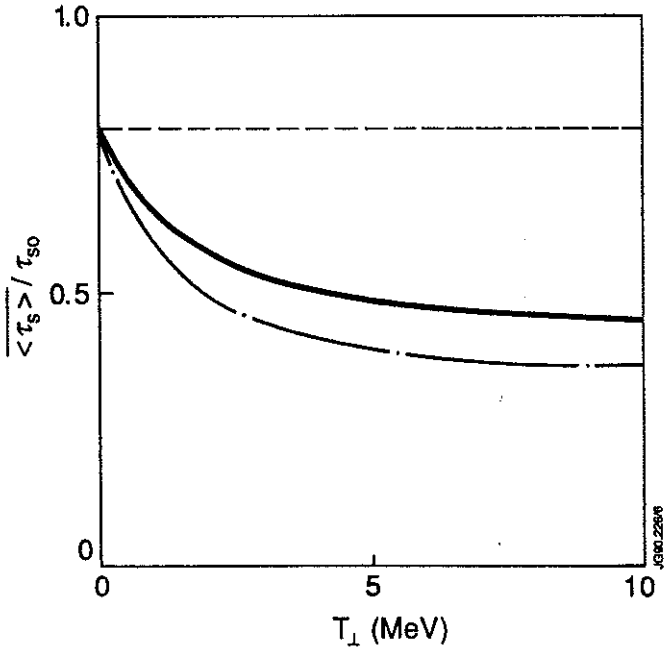

Fig.4. Plotted as a function of tail temperature, $T_\perp$, is the expectation value of the orbit–averaged slowing–down time $\overline{<\tau_S>}$ having been weighted with a typical ICRH high energy tail distribution (Eq.(2.11)). Solid curve: exact guiding–centre orbits; broken curve: approximate circular orbits.

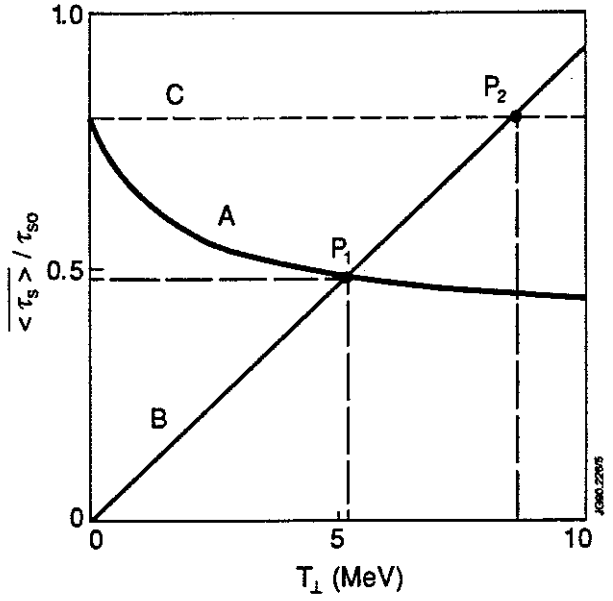

Fig.5. Curve A: expectation value of the orbit–averaged slowing–down time $\overline{<\tau_s>}/\tau_{s0}$ (weighted with a typical ICRH high energy tail distribution as in Fig.4 for the exact guiding–centre orbits) plotted as a function of effective tail temperature, $T_{\perp eff}$. Line B: variation of the effective slowing–down time τ_{sc}/τ_{s0}. The self–consistent finite orbit–width solution is found at the point of intersection P_1 ($\tau_{sc}/\tau_{s0} = 0.47$, $T_{\perp sc} = 5.2$ MeV). A second point of intersection between line B and the horizontal (dashed) zero orbit–width model (line C) occurs at P_1 ($\tau_s/\tau_{s0} = 0.79$, $T_\perp = 8.6$ MeV). Point P_2 represents the normally assumed zero orbit–width solution.

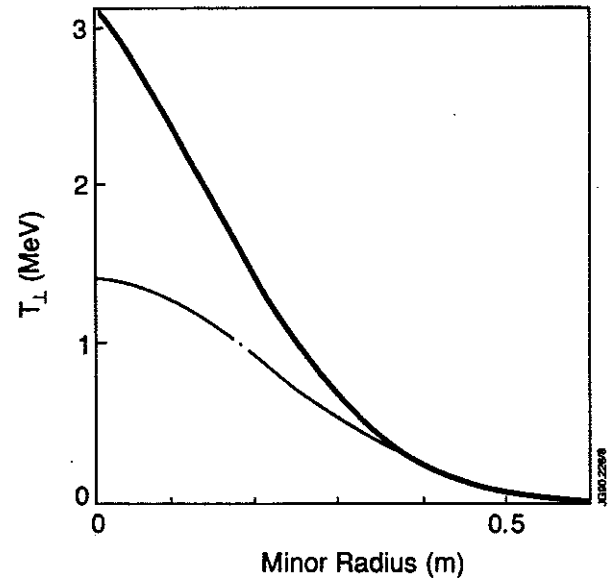

Fig.6. Plot of the radial variation of the asymptotic tail temperature, $T_\perp$, for a 2 MA centrally–heated 2 MA ICRH discharge in the (H)D scheme. Solid curve: zero orbit–width model; broken curve: self–consistent finite orbit–width model.

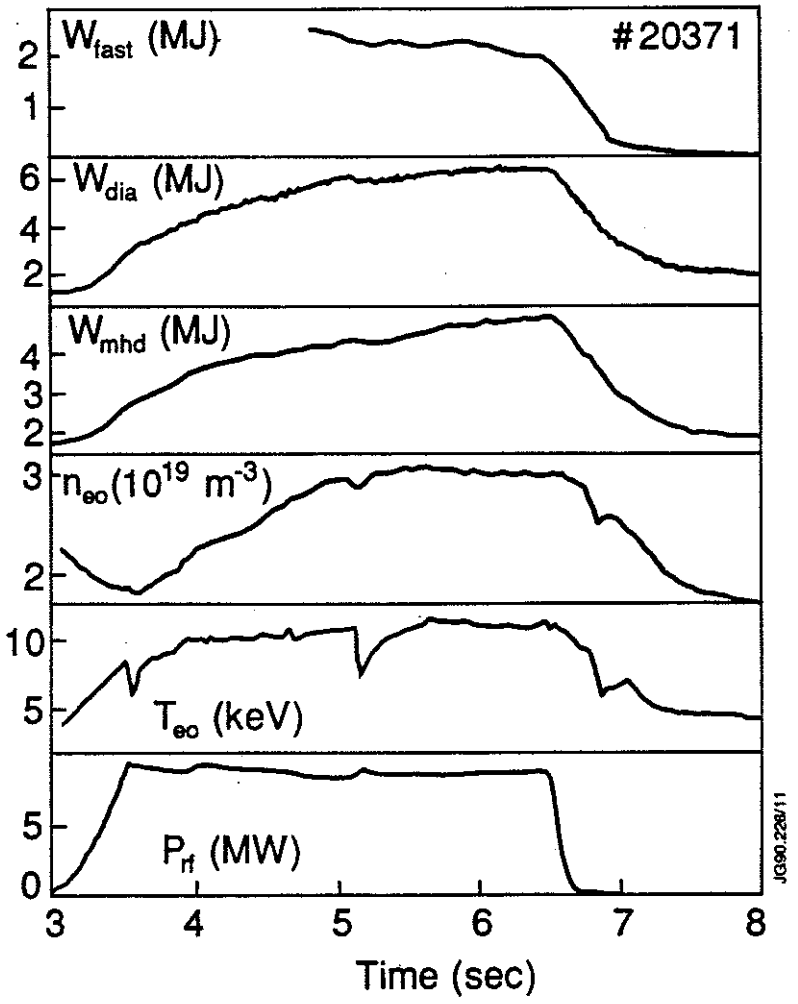

Fig.7. Time evolution of a typical hydrogen minority ICRH heated discharge (I_p = 5 MA, B_φ = 3.1 Tesla) on JET following Be evaporation in the torus. The experimental traces are: coupled ICRH power (P_{rf}), central electron temperature (T_{e_0}), central electron density (n_{e_0}), plasma energy derived from the magnetic equilibrium (W_{mhd}), plasma energy derived from diamagnetism (W_{dia}) and the total anisotropic component of the plasma energy associated with the fast ion component (W_{fast}).

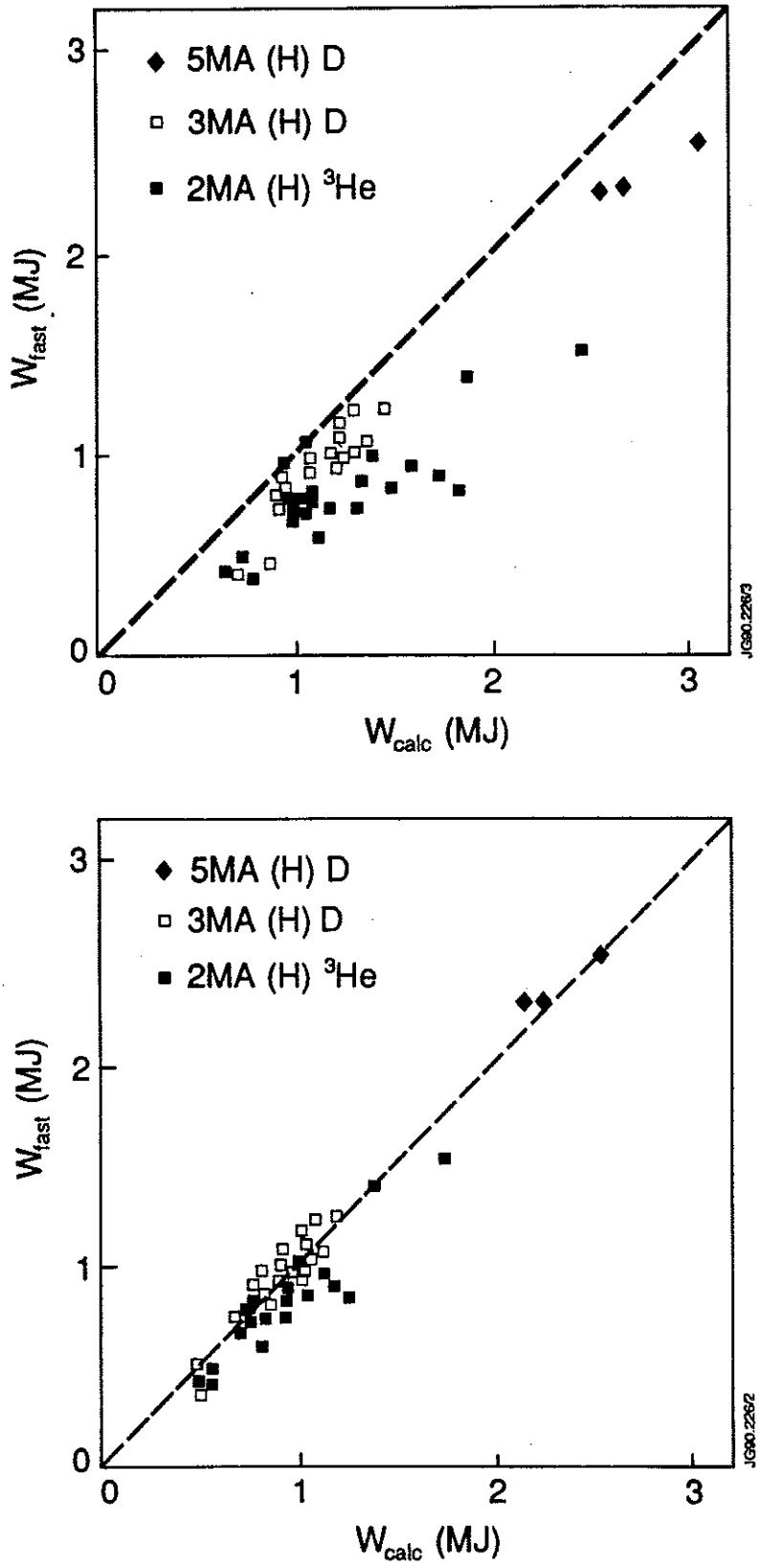

Fig.8.(a) Measured total fast ion energy versus zero orbit–width limit classical prediction (W_{calc}) for a set of centrally–heated, (H)D regime, sawtooth–free plasmas with different plasma currents.(b) The same data compared with the self–consistent finite orbit–width classical model.

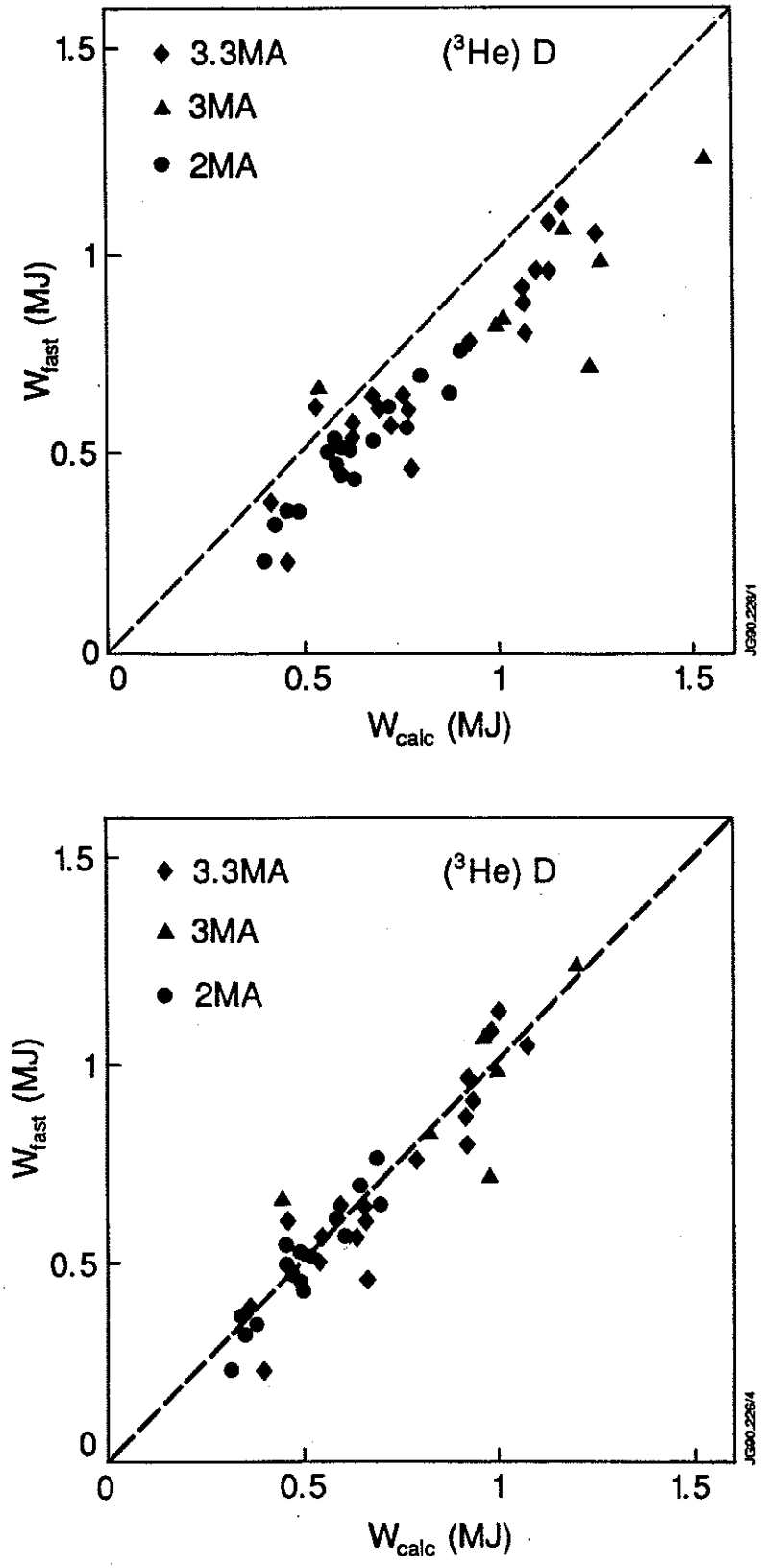

Fig.9.(a) Measured total fast ion energy versus zero orbit–width limit classical prediction (W_{calc}) for a set of centrally–heated, (^{3}He)D regime, sawtooth–free plasmas with different plasma currents. (b) The same data compared with the self–consistent finite orbit–width classsical model. The data have been selected with $P_{rf}/n_{e_0} > 1.5$ MW 10^{-19} m^3.

APPENDIX 1.

THE JET TEAM

JET Joint Undertaking, Abingdon, Oxon, OX14 3EA, U.K.

J.M.Adams[1], F.Alladio[4], H.Altmann, R.J.Anderson, G.Appruzzese, W.Bailey, B.Balet, D.V.Bartlett, L.R.Baylor[24], K.Behringer, A.C.Bell, P.Bertoldi, E.Bertolini, V.Bhatnagar, R.J.Bickerton, A.Boileau[3], T.Bonicelli, S.J.Booth, G.Bosia, M.Botman, D.Boyd[31], H.Brelen, H.Brinkschulte, M.Brusati, T.Budd, M.Bures, T.Businaro[4], H.Buttgereit, D.Cacaut, C.Caldwell-Nichols, D.J.Campbell, P.Card, J.Carwardine, G.Celentano, P.Chabert[27], C.D.Challis, A.Cheetham, J.Christiansen, C.Christodoulopoulos, P.Chuilon, R.Claesen, S.Clement[30], J.P.Coad, P.Colestock[6], S.Conroy[13], M.Cooke, S.Cooper, J.G.Cordey, W.Core, S.Corti, A.E.Costley, G.Cottrell, M.Cox[7], P.Cripwell[13], F.Crisanti[4], D.Cross, H.de Blank[16], J.de Haas[16], L.de Kock, E.Deksnis, G.B.Denne, G.Deschamps, G.Devillars, K.J.Dietz, J.Dobbing, S.E.Dorling, P.G.Doyle, D.F.Düchs, H.Duquenoy, A.Edwards, J.Ehrenberg[14], T.Elevant[12], W.Engelhardt, S.K.Erents[7], L.G.Eriksonn[5], M.Evrard[2], H.Falter, D.Flory, M.Forrest[7], C.Froger, K.Fullard, M.Gadeberg[11], A.Galetsas, R.Galvao[8], A.Gibson, R.D.Gill, A.Gondhalekar, C.Gordon, G.Gorini, C.Gormezano, N.A.Gottardi, C.Gowers, B.J.Green, F.S.Griph, M.Gryzinski[26], R.Haange, G.Hammett[6], W.Han[9], C.J.Hancock, P.J.Harbour, N.C.Hawkes[7], P.Haynes[7], T.Hellsten, J.L.Hemmerich, R.Hemsworth, R.F.Herzog, K.Hirsch[14], J.Hoekzema, W.A.Houlberg[24], J.How, M.Huart, A.Hubbard, T.P.Hughes[32], M.Hugon, M.Huguet, J.Jacquinot, O.N.Jarvis, T.C.Jernigan[24], E.Joffrin, E.M.Jones, L.P.D.F.Jones, T.T.C.Jones, J.Källne, A.Kaye, B.E.Keen, M.Keilhacker, G.J.Kelly, A.Khare[15], S.Knowlton, A.Konstantellos, M.Kovanen[21], P.Kupschus, P.Lallia, J.R.Last, L.Lauro-Taroni, M.Laux[33], K.Lawson[7], E.Lazzaro, M.Lennholm, X.Litaudon, P.Lomas, M.Lorentz-Gottardi[2], C.Lowry, G.Magyar, D.Maisonnier, M.Malacarne, V.Marchese, P.Massmann, L.McCarthy[28], G.McCracken[7], P.Mendonca, P.Meriguet, P.Micozzi[4], S.F.Mills, P.Millward, S.L.Milora[24], A.Moissonnier, P.L.Mondino, D.Moreau[17], P.Morgan, H.Morsi[14], G.Murphy, M.F.Nave, M.Newman, L.Nickesson, P.Nielsen, P.Noll, W.Obert, D.O'Brien, J.O'Rourke, M.G.Pacco-Düchs, M.Pain, S.Papastergiou, D.Pasini[20], M.Paume[27], N.Peacock[7], D.Pearson[13], F.Pegoraro, M.Pick, S.Pitcher[7], J.Plancoulaine, J-P.Poffé, F.Porcelli, R.Prentice, T.Raimondi, J.Ramette[17], J.M.Rax[27], C.Raymond, P-H.Rebut, J.Removille, F.Rimini, D.Robinson[7], A.Rolfe, R.T.Ross, L.Rossi, G.Rupprecht[14], R.Rushton, P.Rutter, H.C.Sack, G.Sadler, N.Salmon[13], H.Salzmann[14], A.Santagiustina, D.Schissel[25], P.H.Schild, M.Schmid, G.Schmidt[6], R.L.Shaw, A.Sibley, R.Simonini, J.Sips[16], P.Smeulders, J.Snipes, S.Sommers, L.Sonnerup, K.Sonnenberg, M.Stamp, P.Stangeby[19], D.Start, C.A.Steed, D.Stork, P.E.Stott, T.E.Stringer, D.Stubberfield, T.Sugie[18], D.Summers, H.Summers[20], J.Taboda-Duarte[22], J.Tagle[30], H.Tamnen, A.Tanga, A.Taroni, C.Tebaldi[23], A.Tesini, P.R.Thomas, E.Thompson, K.Thomsen[11], P.Trevalion, M.Tschudin, B.Tubbing, K.Uchino[29], E.Usselmann, H.van der Beken, M.von Hellermann, T.Wade, C.Walker, B.A.Wallander, M.Walravens, K.Walter, D.Ward, M.L.Watkins, J.Wesson, D.H.Wheeler, J.Wilks, U.Willen[12], D.Wilson, T.Winkel, C.Woodward, M.Wykes, I.D.Young, L.Zannelli, M.Zarnstorff[6], D.Zasche[14], J.W.Zwart.

PERMANENT ADDRESS

1. UKAEA, Harwell, Oxon. UK.
2. EUR-EB Association, LPP-ERM/KMS, B-1040 Brussels, Belgium.
3. Institute National des Récherches Scientifique, Quebec, Canada.
4. ENEA-CENTRO Di Frascati, I-00044 Frascati, Roma, Italy.
5. Chalmers University of Technology, Göteborg, Sweden.
6. Princeton Plasma Physics Laboratory, New Jersey, USA.
7. UKAEA Culham Laboratory, Abingdon, Oxon. UK.
8. Plasma Physics Laboratory, Space Research Institute, Sao José dos Campos, Brazil.
9. Institute of Mathematics, University of Oxford, UK.
10. CRPP/EPFL, 21 Avenue des Bains, CH-1007 Lausanne, Switzerland.
11. Risø National Laboratory, DK-4000 Roskilde, Denmark.
12. Swedish Energy Research Commission, S-10072 Stockholm, Sweden.
13. Imperial College of Science and Technology, University of London, UK.
14. Max Planck Institut für Plasmaphysik, D-8046 Garching bei München, FRG.
15. Institute for Plasma Research, Gandhinagar Bhat Gujat, India.
16. FOM Instituut voor Plasmafysica, 3430 Be Nieuwegein, The Netherlands.
17. Commissiariat à L'Energie Atomique, F-92260 Fontenay-aux-Roses, France.
18. JAERI, Tokai Research Establishment, Tokai-Mura, Naka-Gun, Japan.
19. Institute for Aerospace Studies, University of Toronto, Downsview, Ontario, Canada.
20. University of Strathclyde, Glasgow, G4 ONG, U.K.
21. Nuclear Engineering Laboratory, Lapeenranta University, Finland.
22. JNICT, Lisboa, Portugal.
23. Department of Mathematics, Univeristy of Bologna, Italy.
24. Oak Ridge National Laboratory, Oak Ridge, Tenn., USA.
25. G.A. Technologies, San Diego, California, USA.
26. Institute for Nuclear Studies, Swierk, Poland.
27. Commissiariat à l'Energie Atomique, Cadarache, France.
28. School of Physical Sciences, Flinders University of South Australia, South Australia SO42.
29. Kyushi University, Kasagu Fukuoka, Japan.
30. Centro de Investigaciones Energeticas Medioambientales y Techalogicas, Spain.
31. University of Maryland, College Park, Maryland, USA.
32. University of Essex, Colchester, UK.
33. Akademie de Wissenschaften, Berlin, DDR.

CR 88.49.1A